A Rule-Based Controller to Mitigate DC-Side Second-Order Harmonic Current in a Single-Phase Boost Inverter

Damith B. Wickramasinghe Abeywardana, *Student Member, IEEE*, Branislav Hredzak, *Senior Member, IEEE*, and Vassilios G. Agelidis, *Senior Member, IEEE*

***Abstract*—Single conversion stage DC/AC boost inverters are an attractive solution when integrating energy storage devices, such as a battery, fuel cell, or supercapacitor to a single-phase AC grid. However, a second-order harmonic current ripple appears at the DC side of the inverter increasing the internal heat and losses in the energy storage device and degrading its lifetime. In this paper, a rule-based controller is proposed to reduce such harmonic current ripple component. A key feature and advantage of the proposed controller is its ability to reduce the ripple current amplitude in all four inverter output power operating quadrants without being affected by the capacitor tolerances and the internal resistance of the inductors. Presented experimental results validate the performance of the proposed controller on a single-phase grid-connected DC/AC boost inverter-based battery energy storage system.**

***Index Terms*—Battery, boost inverter, fuel cell, rule-based controller (RBC), second-order harmonic ripple current, supercapacitor.**

I. Introduction

GRID-INTEGRATED energy storage systems (ESSs) have been gaining immense interest especially for single-phase applications [1]–[3]. Energy storage technologies suitable for single-phase applications, such as batteries, fuel cells, and supercapacitors, require DC/AC power conversion to integrate them with the AC grid. The boost inverter topology allows the integration of low-voltage DC sources to an AC grid due to its single stage DC to AC power conversion capability, providing boosting and inversion functions in a single conversion stage and numerous boost inverter-based ESSs were analyzed in the literature [4]–[15]. Depending on the application and energy storage technology, a particular ESS can operate in different operating quadrants. For example, a grid-integrated battery ESS (BESS) should be able to operate in all four quadrants to handle both active and reactive power flow on both directions [1], while a directly grid-connected fuel-cell system needs to be operated in the first and the second quadrants only avoiding power flow into the fuel cell [4].

Manuscript received October 16, 2014; revised December 18, 2014 and February 25, 2015; accepted March 29, 2015. Date of publication April 10, 2015; date of current version September 29, 2015. Recommended for publication by Associate Editor D. Xu.

The authors are with the School of Electrical Engineering and Telecommunications, University of New South Wales, Sydney, N.S.W. 2052, Australia (e-mail: d.wickramasingheabeywardana@student.unsw.edu.au; b.hredzak@unsw.edu.au; vassilios.agelidis@unsw.edu.au).

Color versions of one or more of the figures in this paper are available online at http://ieeexplore.ieee.org.

Digital Object Identifier 10.1109/TPEL.2015.2421494

However, the single-phase conversion from DC to AC using the boost inverter topology introduces a second-order harmonic ripple current at the DC side of the converter, and hence, any DC source has to handle this ripple current component. The effect of the low-frequency current ripple on DC ESSs has been analyzed in the technical literature extensively. The impact of such ripple on fuel-cell ESS was reported in [5] and [6], and showed that the low-frequency ripple current can increase the fuel cell losses and results in fuel wastage as well as reduced lifetime. Ruddell [7] showed that the low-frequency ripple current can considerably degrade the lifetime of a lead acid battery due to internal heating. Furthermore, Bala [8] reported a noticeable temperature increment in a lithium–iron–phosphate-battery-based community ESS, as a result of the low-frequency ripple current component. Due to their high-power capability and extended cycle life, supercapacitors have become popular in many hybrid ESSs [9], [10]. However, [11] showed that a supercapacitor can also overheat when exposed to a continuous ripple current which in turn leads to the reduction of its lifetime.

A number of second-order harmonic ripple current reduction methods for the single-phase boost inverter topology have been proposed in the technical literature [12]–[19] and can be classified into passive and active ripple current reduction methods. In the passive methods, a separate energy storage component is added to the converter to supply the second-order harmonic current component, while in the active methods, a control or modulation scheme is introduced to reduce the ripple current component without incurring additional hardware. In [12], [13], authors proposed a separate battery storage to compensate the second-order harmonic ripple current in a boost inverter-based fuel-cell ESS. However, the method required additional hardware and cost. A supercapacitor was employed to supply the second-order harmonic ripple current in the battery–supercapacitor hybrid ESS proposed in [19]. However, according to [11], second-order harmonic ripple current can adversely affect the supercapacitor as well. In the case of active methods, a waveform control (WFC) technique was studied in [15]–[17] for a boost inverter-based fuel-cell ESS, and Guo-Rong [16] reported a noticeable efficiency increase in the ESS due to the second-order harmonic ripple current reduction. However, the method has to be redesigned every time the load changes. A current feedback method for the boost inverter waveform controller to deal with the changing load conditions was proposed in [14]. However, only the unity power factor operation was considered limiting its applicability for a boost inverter ESS, which is

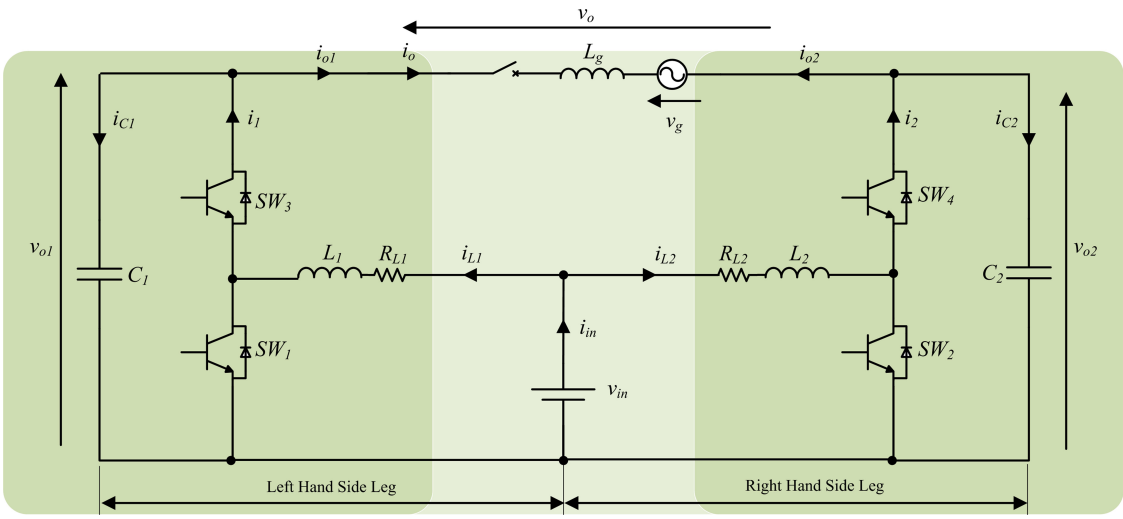

Fig. 1. Single-phase grid-connected BESS.

required to operate in all four output power quadrants. The WFC method was extended to all possible output power conditions in [18]. In [14]–[18], the compensation signal parameters were calculated using an ideal boost inverter model. Hence, the effectiveness of the second-order harmonic ripple reduction was affected by the capacitance tolerance of the inverter output capacitors. In addition, the WFC method cannot compensate for the effect of the internal resistance of the inductors on the ripple. Also, the WFC method in [14]–[18] is not directly applicable to a grid-connected boost inverter because in the grid-connected inverter, the output power control is achieved by changing the inverter output voltage with respect to the grid voltage [13].

Various active ripple current reduction methods were proposed in the literature for two-stage DC/AC converter-based ESSs. A ripple current reduction method using a double-loop controller was proposed in [20]. Second-order harmonic ripple current reduction method was analyzed using a back-current gain transfer function in [21]. An impedance modification method for the second-order harmonic ripple reduction was reported in [22]. However, these methods were specifically designed for the two-stage DC/AC power converter topology. Since the boost inverter topology has a unique operating behavior due to its differential output voltage, the active ripple current reduction methods proposed in [20]–[22] cannot be applied directly to this topology.

In this paper, the WFC method-based ripple current reduction is extended to the grid-connected operation and the effects of the capacitor tolerances and the internal resistance of the inductors on its effectiveness are analyzed. Then, a rule-based controller (RBC) is proposed to reduce the second-order harmonic ripple current in the boost inverter-based ESS. The main advantage of the proposed controller is that it can reduce the second-order harmonic ripple current in all four output power quadrants without being affected by the capacitor tolerances and the internal resistance of the inductors. The effectiveness of the proposed controller is experimentally verified on a single-phase grid-connected DC/AC boost inverter-based battery ESS prototype and it is shown that its performance is superior when compared with the WFC method.

The remainder of this paper is organized as follows. The basic operation of the grid-connected boost inverter, WFC method for a grid-connected boost inverter, and the effect of the capacitor tolerances and the inductor internal resistance on the WFC method performance are discussed in Section II. Section III describes the operation of the proposed RBC for the boost inverter DC-side ripple current reduction. The boost inverter controller design is explained in Section IV, while experimental results are presented and discussed in Section V. Finally, the conclusions of this paper are summarized in Section VI.

II. Operation of the Grid-Connected Boost Inverter and Ripple Current Reduction

A. Overview

The configuration of the grid-connected boost inverter is shown in Fig. 1. The converter average model describes its dynamic behavior [23]. The model equations for the left-hand side boost converter leg can be expressed as follows:

$$v_{\text{in}} - v_{L1} = (1 - d_1)v_{o1} \tag{1}$$

$$i_{C1} + i_{o1} = (1 - d_1)i_{L1} \tag{2}$$

where v_{o1} and i_{C1} are the voltage and current of the capacitor C_1, and v_{L1} and i_{L1} are the voltage and current of the inductor L_1. v_{in} is the input voltage to the boost inverter, whereas d_1 is the duty cycle time average value of the switch SW_1. Subscript 1 denotes the left-hand side boost converter leg and i_{o1} is the output current of the left-hand side boost converter leg. The inductor and capacitor differential equations are

$$v_{L1} = R_{L1}i_{L1} + L_1 di_{L1}/dt \tag{3}$$

$$i_{C1} = C_1 dv_{o1}/dt. \tag{4}$$

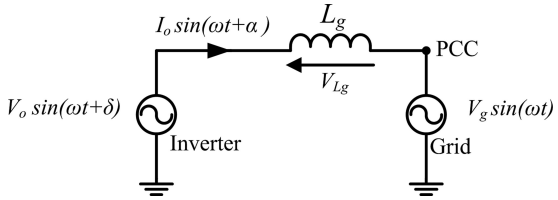

Fig. 2. Generic equivalent circuit of a grid-connected inverter linked to the AC grid through a lossless inductor.

The objective of the boost inverter is to supply a sinusoidal voltage v_o which follows the reference voltage

$$v_{o,\mathrm{ref}} = V_o \sin(\omega t + \delta) \tag{5}$$

where V_o, ω, and δ are the amplitude, frequency, and phase angle of the inverter output voltage, respectively. In order to obtain the required differential output voltage, the left-hand side boost converter leg and the right-hand side boost converter leg are required to follow independent voltage references $v_{o1,\mathrm{ref}}$ and $v_{o2,\mathrm{ref}}$ across the output capacitors C_1 and C_2

$$v_{o1,\mathrm{ref}} = V_d + v_{o,\mathrm{ref}}/2 \tag{6}$$

$$v_{o2,\mathrm{ref}} = V_d - v_{o,\mathrm{ref}}/2. \tag{7}$$

The voltage references $v_{o1,\mathrm{ref}}$ and $v_{o2,\mathrm{ref}}$ have a DC shift V_d given by (8), where v_{in} is the input voltage to the boost inverter

$$V_d \geq v_{\mathrm{in}} + V_o/2. \tag{8}$$

The boost inverter can be integrated to a single-phase grid using an interfacing inductor L_g as shown in Fig. 1. The equivalent circuit of the grid-connected inverter is shown in Fig. 2. In the figure, V_g, V_o, and δ are the grid voltage amplitude, inverter output voltage amplitude, and phase angle of the inverter voltage with respect to the phase angle of the grid voltage. For small δ values, the active power (P) and the reactive power (Q) exchanged with the grid can be approximated as [24]

$$P \approx \frac{V_g V_o}{2\omega L_g}\delta \tag{9}$$

$$Q \approx \frac{V_g(V_o - V_g)}{2\omega L_g}. \tag{10}$$

Hence, by proper control of the inverter output voltage amplitude and phase angle with respect to the grid voltage, the active and reactive power flow between the grid and the inverter can be achieved [24].

B. Second-Order Harmonic Input Ripple Current Component in the Boost Inverter

The inverter output current i_o is given by

$$i_o = I_o \sin(\omega t + \alpha) \tag{11}$$

where α is the phase angle of the inverter output current with respect to the grid voltage. The output capacitor currents i_{C1}, i_{C2} are

$$i_{C1} = C_1 \omega \frac{V_o}{2} \cos(\omega t + \delta) \tag{12}$$

$$i_{C2} = -C_2 \omega \frac{V_o}{2} \cos(\omega t + \delta). \tag{13}$$

Using (4)–(6), (11), and (12)

$$i_1 = I_o \sin(\omega t + \alpha) + C_1 \omega \frac{V_o}{2} \cos(\omega t + \delta). \tag{14}$$

Similarly, i_2 can be written as

$$i_2 = -I_o \sin(\omega t + \alpha) - C_2 \omega \frac{V_o}{2} \cos(\omega t + \delta). \tag{15}$$

Then, using (1), (2), and neglecting losses and energy stored in the inductors

$$i_{\mathrm{in}} = i_1 \frac{v_{o1}}{v_{\mathrm{in}}} + i_2 \frac{v_{o2}}{v_{\mathrm{in}}}. \tag{16}$$

The total input current to the boost inverter can then be obtained as

$$i_{\mathrm{in}} = \frac{1}{v_{\mathrm{in}}} \left[\frac{V_o I_o}{2} \cos(\alpha - \delta) + \frac{V_o}{2} \sqrt{\left[I_o^2 + \frac{C^2\omega^2 V_o^2}{4} + V_o I_o C\omega \sin(\alpha - \delta) \right]} . \cos(2\omega t - \theta) \right] \tag{17}$$

where

$$\cos\theta = \frac{-I_o \cos(\alpha + \delta) + \frac{C\omega V_o \sin(2\delta)}{2}}{\sqrt{\left[I_o^2 + \frac{C^2\omega^2 V_o^2}{4} + V_o I_o C\omega \sin(\alpha - \delta) \right]}}$$

and $C = C_1 = C_2$.

The magnitude and phase angle of the second-order harmonic ripple component depend on the inverter output current and the phase angle and, hence, depend on the inverter output power.

The inductor currents i_{L1} and i_{L2} are

$$i_{L1} = A_{\omega,n} \cos(\omega t + \lambda_{\omega,n}) + A_{2\omega,n} \cos(2\omega t + \lambda_{2\omega,n}) \tag{18}$$

$$i_{L2} = -A_{\omega,n} \cos(\omega t + \lambda_{\omega,n}) + A_{2\omega,n} \cos(2\omega t + \lambda_{2\omega,n}) \tag{19}$$

where

$$A_{\omega,n} = \frac{1}{v_{\mathrm{in}}} \sqrt{(I_o V_d)^2 + \left(\frac{C\omega V_o V_d}{2} \right)^2 + I_o V_d^2 V_o C\omega \sin(\alpha - \delta)}$$

$$A_{2\omega,n} = \frac{V_o}{4v_{\mathrm{in}}} \sqrt{I_o^2 + \frac{C^2\omega^2 V_o^2}{4} + V_o I_o C\omega \sin(\alpha - \delta)}$$

$$\cos\lambda_{\omega,n} = \frac{I_o V_d \sin\alpha + \frac{C\omega V_o V_d \cos\delta}{2}}{\sqrt{(I_o V_d)^2 + \left(\frac{C\omega V_o V_d}{2}\right)^2 + I_o V_d^2 V_o C\omega \sin(\alpha - \delta)}}$$

and

$$\cos\lambda_{2\omega,n} = \frac{-I_o\cos(\alpha+\delta) + \frac{C\omega V_o\sin(2\delta)}{2}}{\sqrt{I_o^2 + \frac{C^2\omega^2V_o^2}{4}} + V_oI_oC\omega\sin(\alpha-\delta)}.$$

From (12), (13), (18), and (19), it is clear that the second-order harmonic current components flow only through the inductors and not through the output capacitors [16].

C. Second-Order Harmonic Input Current Ripple Reduction Using WFC Method

In [16], a WFC method was proposed to reduce the second-order harmonic input current ripple of a boost inverter, which was operated at a unity power factor. Operation of the WFC method was extended for all possible power factor conditions in [18]. In this paper, the analysis of the WFC method is extended to a grid-connected boost inverter where the inverter output power is controlled by modifying the inverter output voltage amplitude and phase angle. Since the boost inverter is a differential inverter, the output capacitor voltages v_{o1} and v_{o2} can be modified as in (20) and (21), without affecting the required inverter output voltage given by (5)

$$v_{o1} = V_d + \frac{V_o}{2}\sin(\omega t+\delta) + B\sin(2\omega t+\varphi) \quad (20)$$

$$v_{o2} = V_d - \frac{V_o}{2}\sin(\omega t+\delta) + B\sin(2\omega t+\varphi) \quad (21)$$

where B is the amplitude of the second-order harmonic voltage component and φ is the phase angle of the second-order harmonic voltage component with respect to the grid voltage.

Then, the output capacitor currents can be written as

$$i_{C1} = C\omega\frac{V_o}{2}\cos(\omega t+\delta) + 2BC\omega\cos(2\omega t+\varphi) \quad (22)$$

$$i_{C2} = -C\omega\frac{V_o}{2}\cos(\omega t+\delta) + 2BC\omega\cos(2\omega t+\varphi). \quad (23)$$

The total input current with the modified output capacitor voltages as in (20) and (21) can be written as

$$i_{\rm in} = \frac{V_oI_o}{2v_{\rm in}}\cos(\alpha-\delta) + \frac{V_o}{2v_{\rm in}}\sqrt{\left[I_o^2+\frac{C^2\omega^2V_o^2}{4}+V_oI_oC\omega\sin(\alpha-\delta)\right]}.\cos(2\omega t-\theta) + \frac{4\omega BCV_d\cos(2\omega t+\varphi)}{v_{\rm in}} + \frac{2\omega B^2C\sin(4\omega t+2\varphi)}{v_{\rm in}} \quad (24)$$

where

$$\cos\theta = \frac{-I_o\cos(\alpha+\delta) + \frac{C\omega V_o}{2}\sin(2\delta)}{\sqrt{\left[I_o^2 + \frac{C^2\omega^2V_o^2}{4} + V_oI_oC\omega\sin(\alpha-\delta)\right]}}.$$

The first term of (24) is the DC component of the input current which corresponds to the inverter output power. The second term is the uncompensated second-order harmonic ripple current component of the boost inverter. The second-order harmonic ripple current component due to the second-order harmonic output capacitor voltage reference component is given by the third term of the equation. It can be observed that due to the modification of the output capacitor reference voltages, a fourth-order harmonic ripple component is also present in the input current (the fourth term in (24)). By selecting B and φ such that

$$\frac{V_o}{2}\sqrt{\left[I_o^2 + \frac{C^2\omega^2V_o^2}{4} + V_oI_oC\omega\sin(\alpha-\delta)\right]}.\cos(2\omega t-\theta) + 4\omega BCV_d\cos(2\omega t+\varphi) = 0 \quad (25)$$

the second-order harmonic ripple component of the input current can be theoretically eliminated. The parameters B and φ, which satisfy (25) are given by

$$B = \frac{V_o}{8V_d\omega C}\sqrt{\left[I_o^2 + \frac{C^2\omega^2V_o^2}{4} + V_oI_oC\omega\sin(\alpha-\delta)\right]} \quad (26)$$

and

$$\cos(\varphi) = \frac{I_o\cos(\delta+\alpha) - \frac{C\omega V_o}{2}\sin(2\delta)}{\sqrt{\left[I_o^2 + \frac{C^2\omega^2V_o^2}{4} + V_oI_oC\omega\sin(\alpha-\delta)\right]}}. \quad (27)$$

D. Effect of the WFC Method on the Inductor Current Harmonic Content and Efficiency

With the WFC method, the inductor currents i_{L1} and i_{L2} can be written as

$$\begin{aligned} i_{L1} = {} & A_{\omega,n}\cos(\omega t+\lambda_{\omega,n}) + A_{\omega,w}\cos(\omega t+\lambda_{\omega,w}) \\ & + A_{2\omega,n}\cos(2\omega t+\lambda_{2\omega,n}) + A_{2\omega,w}\cos(2\omega t+\lambda_{2\omega,w}) \\ & + A_{3\omega,w}\cos(3\omega t+\lambda_{3\omega,w}) \\ & + A_{4\omega,w}\sin(4\omega t+\lambda_{4\omega,w}) \end{aligned} \quad (28)$$

$$\begin{aligned} i_{L2} = {} & -A_{\omega,n}\cos(\omega t+\lambda_{\omega,n}) - A_{\omega,w}\cos(\omega t+\lambda_{\omega,w}) \\ & + A_{2\omega,n}\cos(2\omega t+\lambda_{2\omega,n}) + A_{2\omega,w}\cos(2\omega t+\lambda_{2\omega,w}) \\ & - A_{3\omega,w}\cos(3\omega t+\lambda_{3\omega,w}) \\ & + A_{4\omega,w}\sin(4\omega t+\lambda_{4\omega,w}) \end{aligned} \quad (29)$$

where

$$A_{\omega,w} = \frac{1}{v_{\rm in}}\sqrt{\left(\frac{BI_o}{2}\right)^2 + \left(\frac{BC\omega V_o}{4}\right)^2 - \frac{B^2V_oI_oC\omega\sin(\alpha-\delta)}{4}}$$

$$A_{2\omega,w} = \frac{2BC\omega V_d}{v_{\rm in}}$$

$$A_{3\omega,w} = \frac{1}{v_{\rm in}}\sqrt{\left(\frac{3BV_oC\omega}{4}\right)^2 + \left(\frac{BI_o}{2}\right)^2 + \frac{3B^2V_oI_oC\omega\sin(\alpha-\delta)}{4}}$$

$$A_{4\omega,w} = \frac{B^2C\omega}{v_{\rm in}}$$

TABLE I
ESS EXPERIMENTAL PROTOTYPE PARAMETERS

Parameter	Value	PARAMETER	Value
Power converter parameters			
V_o	40 V	f	50 Hz
C_1,C_2	60 μF	L_1,L_2	210 μH
$I_{o,\max}$	1.5 A	T_F	0.001
V_d	42 V	$f_{\rm sw}$	20 kHz
Grid parameters			
V_g	40 V	L_g	20 mH
Voltage control loop parameters			
$K_{p,\rm PR}$	0.1	$K_{i2,\rm PR}$	6
$K_{i1,\rm PR}$	4	ω_{c1}, ω_{c2}	0.5
Current control loop parameters			
$K_{p,\rm PI}$	2.615	$K_{i,\rm PI}$	8.44×10^{-5}
Proposed RBC parameters			
N_B	1.1	$N\varphi$	0.25
$T_{\rm avg}$	0.02 s	T_D	0.03 s
ε	0.01		

$$\cos\lambda_{\omega,w} = \frac{\frac{BI_o}{2}\cos(\varphi-\alpha) - \frac{BV_oC\omega}{4}\sin(\varphi-\delta)}{\sqrt{\left(\frac{BI_o}{2}\right)^2 + \left(\frac{BC\omega V_o}{4}\right)^2 - \frac{B^2V_oI_oC\omega\sin(\alpha-\delta)}{4}}}$$

$$\cos\lambda_{2\omega,w} = \cos\varphi$$

$$\cos\lambda_{3\omega,w} = \frac{\frac{3BV_oC\omega}{4}\sin(\varphi+\delta) - \frac{BI_o}{2}\cos(\alpha+\varphi)}{\sqrt{\left(\frac{3BV_oC\omega}{4}\right)^2 + \left(\frac{BI_o}{2}\right)^2 + \frac{3B^2V_oI_oC\omega\sin(\alpha-\delta)}{4}}}$$

and

$$\cos\lambda_{4\omega,w} = \cos 2\varphi.$$

In (28) and (29), the subscripts "*n*" and "*w*" denote the amplitude and phase-angle components during the normal operation (without the WFC) and the operation with the WFC method, respectively. The second-order harmonic components of the inductor currents (28), (29) can be rewritten as

$$i_{L_{1,2},2\omega} = \frac{V_o}{4}\sqrt{\left[I_o^2 + \frac{C^2\omega^2V_o^2}{4} + V_oI_oC\omega\sin(\alpha-\delta)\right]} \cdot\cos(2\omega t-\theta) + 2\omega BCV_d\cos(2\omega t+\varphi). \quad (30)$$

Then, by selecting *B* and φ as in (26) and (27), the second-order harmonic components of the inductor currents can be theoretically eliminated and will only flow through the output capacitors as evident from (22) and (23).

The frequency content of the inductor current without and with the WFC method can be obtained from (18) and (28) using the prototype parameters given in Table I. Fig. 3 illustrates the frequency content of the inductor current when the boost inverter supplies 10 W active power and 15 V Ar reactive power to the grid. With the WFC, the fundamental frequency component shows a slight reduction, the second-order harmonic component is completely eliminated and the third-order and fourth-order harmonic components are negligible. Since with the WFC the second-order harmonic current is eliminated from the inductor and allocated to the output capacitor, the power loss in the inductor is reduced which in turn increases the converter efficiency as presented in [16] and [25].

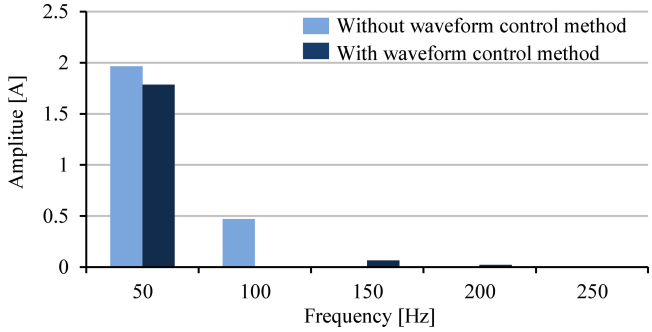

Fig. 3. Frequency content of the inductor current i_{L1}, without and with the WFC method when delivering 10 W active power and 15 V Ar reactive power to the grid.

E. Selection of the Output Capacitor Capacitance C

From the analysis shown in Section IV, it is obvious that due to the WFC method, the output capacitors of the boost inverter have to supply the second-order harmonic power variation as opposed to the normal boost inverter operation in which the second-order harmonic power variation is supplied by the input power source. In the following paragraphs, this effect is analyzed and it is shown how it affects the selection of the required output capacitor capacitance as compared with the selection of the capacitance for the normal operation.

During operation with the WFC, the maximum value of *B*, $B_{\max}$, can be found from (26) for the maximum output current $I_{o,\max}$ as

$$B_{\max} = \frac{V_o}{8V_d\omega C}\sqrt{(I_{o,\max})^2 + \frac{C^2\omega^2V_o^2}{4} + V_oI_{o,\max}C\omega}. \quad (31)$$

Then, the maximum and minimum values of the output capacitor voltages are

$$v_{o1,\max} = V_d + \frac{V_o}{2} + B_{\max} \quad (32)$$

$$v_{o1,\min} = V_d - \frac{V_o}{2} - B_{\max}. \quad (33)$$

In addition, V_d has to satisfy the inequality

$$V_d > v_{\rm in} + \frac{V_o}{2} + B_{\max}. \quad (34)$$

$$V_{d,\min} = \frac{1}{2}\left[v_{\rm in} + \frac{V_o}{2} + \sqrt{\left(v_{\rm in}+\frac{V_o}{2}\right)^2 + \left(\frac{V_o}{2\omega C}\sqrt{(I_{o,\max})^2 + \frac{C^2\omega^2V_o^2}{4}} + V_oI_{o,\max}C\omega\right)}\right] \quad (35)$$

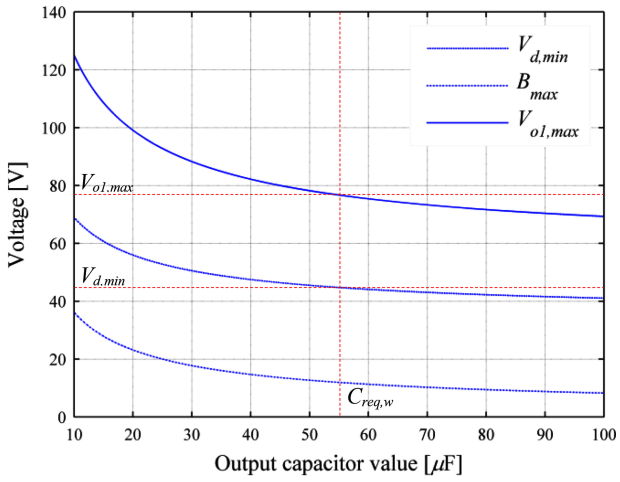

Fig. 4. Relationships between $B_{\max}$, $v_{o1,\max}$, and $V_{d,\min}$ versus the output capacitor C values during operation with the WFC.

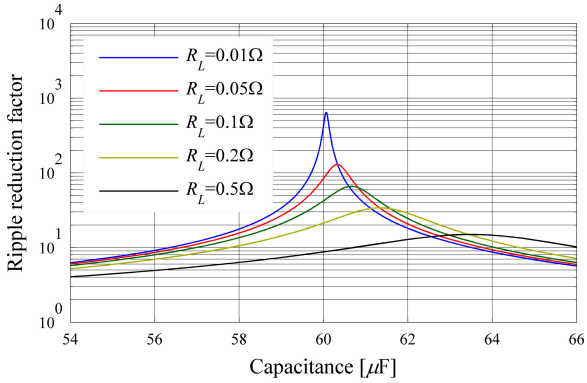

Fig. 5. Ripple reduction factor for various values of the inductor resistance R_L and capacitance C of the output capacitors when the WFC method is used (inverter supplies 10 W active power and 15 V Ar reactive power).

From (32), it is clear that the higher the V_d, the higher the amplitude of the maximum output capacitor reference voltage $V_{o1,\max}$. Since a low value of V_d is preferred to reduce the gain of the boost inverter, a minimum possible value of V_d, $V_{d,\min}$, which satisfies (34) can be obtained from (31) and (34) as, (35) as shown bottom of the previous page.

Substituting $V_d = V_{d,\min}$ in (30), the maximum value of the output capacitor voltages $V_{o1.\max}$ is

$$V_{o1,\max} = V_{d,\min} + \frac{V_o}{2} + B_{\max}. \tag{36}$$

The relationship of $V_{d,\min}$, $B_{\max}$, and $V_{o1,\max}$ versus the output capacitance value C for $I_{o,\max} = 1.5$ A is shown in Fig. 4. From Fig. 4, it can be observed that higher C leads to lower $B_{\max}$, $V_{d,\min}$, and $V_{o1,\max}$. Hence, the required output capacitor capacitance value $C_{\text{req},w}$ can be found as follows. First, the maximum allowable output capacitor voltage $V_{o1,\max}$ is predetermined from the input voltage v_{in} and the maximum gain of the converter legs $G_{\max}$, as $V_{o1,\max} = v_{\text{in}} \times G_{\max}$. Next, using (31), (35), and (36), values of $B_{\max}$, $V_{d,\min}$, and $V_{o1,\max}$ are plotted against a range of the output capacitor C values. Then, for the predetermined $V_{o1,\max}$ value, both the required output capacitor capacitance value $C_{\text{req},w}$ and the required output capacitor reference voltage minimum DC shift $V_{d,\min}$ can be obtained graphically as illustrated in Fig. 4.

When considering the normal operation (without the WFC method), the DC shift voltage V_d has to satisfy the inequality

$$V_d \geq v_{\text{in}} + \frac{V_o}{2}. \tag{37}$$

Hence, the minimum possible DC shift $V_{d,\min}$ is

$$V_{d,\min} = v_{\text{in}} + \frac{V_o}{2} \tag{38}$$

and the maximum output capacitor voltage $V_{o1,\max}$ is

$$V_{o1,\max} = V_d + \frac{V_o}{2}. \tag{39}$$

From (38) and (39), it is clear that $V_{d,\min}$ and $V_{o1,\max}$ are independent of the output capacitor value C. Therefore, during the normal boost inverter operation, the required output capacitor value $C_{\text{req},n}$ can be found from a selected maximum switching frequency voltage ripple in the output capacitor voltage waveform $\Delta V_{o1,\max}$, which is given by

$$\Delta V_{o1,\max} = \frac{I_{o,\max} d_{1,\max}}{f_{\text{sw}} C_{\text{req},n}} \tag{40}$$

where

$$d_{1,\max} = \frac{V_{o1,\max} - v_{\text{in}}}{V_{o1,\max}} \tag{41}$$

assuming a lossless conversion. From (40) and (41), the required output capacitor value $C_{\text{req},n}$ during the normal operation is

$$C_{\text{req},n} = \frac{I_{o,\max}}{f_{\text{sw}} \Delta V_{o1,\max}} \frac{V_{o1,\max} - v_{\text{in}}}{V_{o1,\max}}. \tag{42}$$

The following example illustrates the selection of the required output capacitor values $C_{\text{req},n}$ and $C_{\text{req},w}$ for the normal operation and operation with the WFC, respectively.

Consider a boost inverter with the input voltage v_{in}, the output voltage peak value V_o and the maximum peak output current $I_{o,\max}$ is equal to 12.8 V, 40 V, and 1.5 A, respectively. Assume that the switching frequency of the converter is 20 kHz and the maximum gain of the boost converter leg $G_{\max}$ is 6. Then, according to (39), the maximum output capacitor voltage $V_{o1,\max}$ for the normal operation is 52.8 V which corresponds to the converter leg gain G equal to 4.125. If the required output capacitor switching frequency ripple $\Delta V_{o1,\max}$ is less than 5% of the peak output voltage ($\Delta V_{o1,\max} = 40 \times 5\,\% = 2$ V) then the required output capacitor value $C_{\text{req},n}$ for the normal operation can be calculated from (42) as 28.4 μF.

If the value of $C_{\text{req},n}$ found for the normal operation is used with the WFC method, then the required peak output capacitor voltage $V_{o1,\max}$ can be obtained from Fig. 4 as 89.56 V. However, to achieve this voltage, the converter leg gain G has to be equal to 7. Since this gain exceeds the maximum possible gain $G_{\max}$, the $C_{\text{req},n}$ value cannot be used with the WFC method and the $C_{\text{req},w}$ value has to be found as follows. Considering the maximum gain of the boost converter leg $G_{\max} = 6$, the maximum possible output capacitor voltage $V_{o1,\max}$ is 76.8 V.

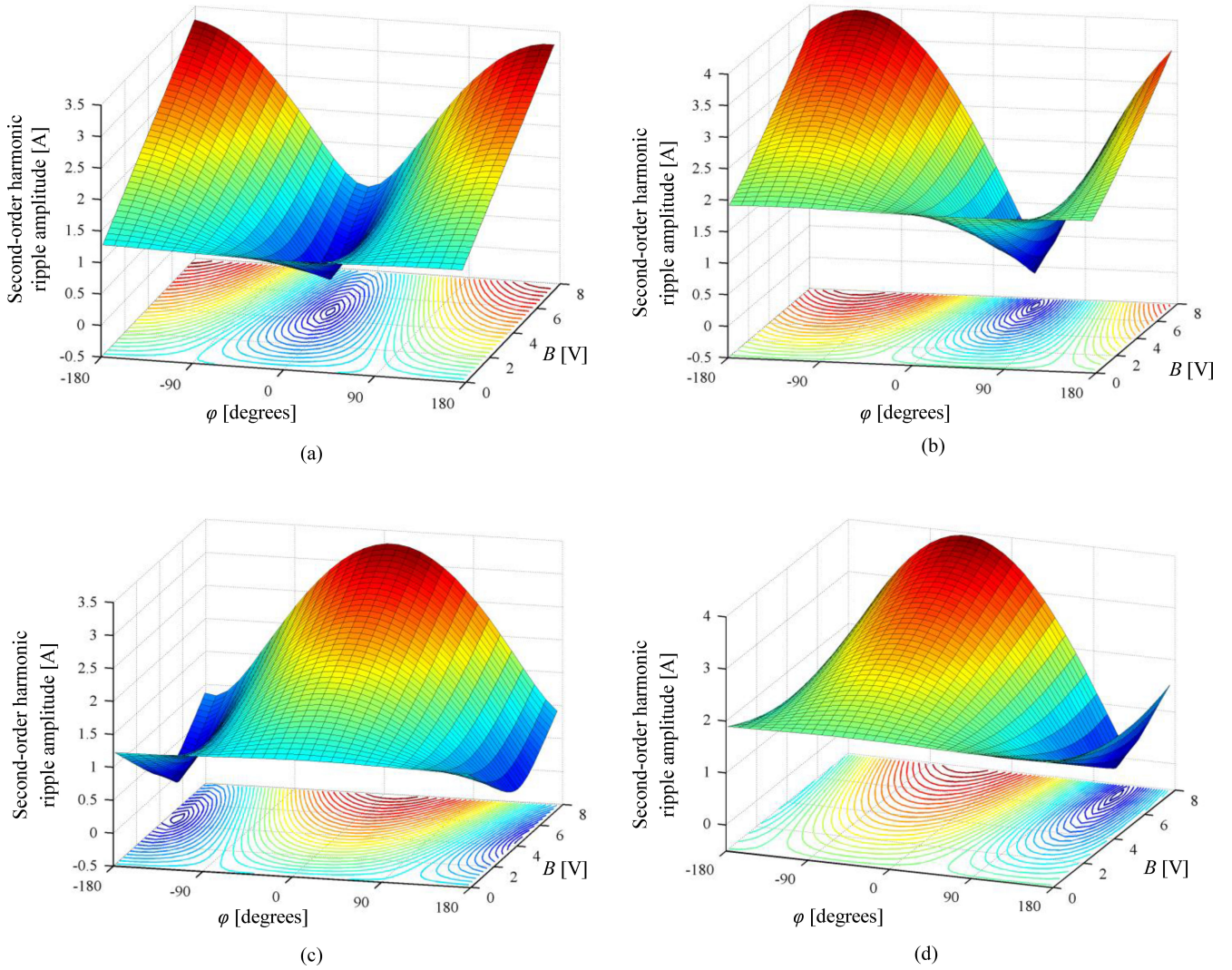

Fig. 6. Second-order harmonic ripple current amplitude as a function of B and φ when (a) inverter supplies 15 W active power and 10 V Ar reactive power, (b) inverter supplies 15 W active power and absorbs 10 V Ar reactive power, (c) inverter absorbs 15 W active power and supplies 10 V Ar reactive power, and (d) inverter absorbs 15 W active power and 10 V Ar reactive power.

Then, the required output capacitor value $C_{\mathrm{req},w}$ to maintain the output capacitor peak voltage less than 76.8 V can be obtained from Fig. 4 as $C_{\mathrm{req},w} = 54.6\ \mu$F. The nearest comercially available value of 60 μF is then selected in the actual setup.

F. Effect of the Capacitor Tolerances and the Inductor Resistance on the WFC Method Performance

In the WFC method, (26) and (27) are used to calculate the required second-order harmonic output capacitor voltage reference signal to reduce the second-order harmonic input ripple current. However, in the derivation of (26) and (27), the internal resistances of the boost inverter inductors are neglected for simplicity. Moreover, since the second-order harmonic voltage reference amplitude B and phase angle φ are functions of the capacitance of the output capacitor, the effect of the output capacitor tolerances on the ripple reduction using the WFC method has to be investigated. In order to analyze the effect of the internal resistance of the inductors and the capacitor tolerances on the total input current, the inductor currents of the boost inverter can be written as

$$i_{L1} = \frac{i_1 v_{o1}}{v_{\mathrm{in}} - i_{L1} R_{L1}}, \qquad i_{L2} = \frac{i_2 v_{o2}}{v_{\mathrm{in}} - i_{L2} R_{L2}}. \tag{43}$$

Then, the total input current can be obtained from

$$i_{\mathrm{in}} = \frac{v_{\mathrm{in}} - \sqrt{(v_{\mathrm{in}}^2 - 4R_L v_{o1} i_1)}}{2R_L} + \frac{v_{\mathrm{in}} - \sqrt{(v_{\mathrm{in}}^2 - 4R_L v_{o2} i_2)}}{2R_L} \tag{44}$$

where $R_L = R_{L1} = R_{L2}$.

The effect of the internal resistance of the inductors and tolerance of the capacitors on the total input current can be observed by simulating (44). Inverter parameters equal to the prototype parameters summarized in Table I are used in the analysis. First, the second-order output capacitor voltage reference parameters are calculated from (26) and (27) using $C = 60\ \mu$F. Then, (44)

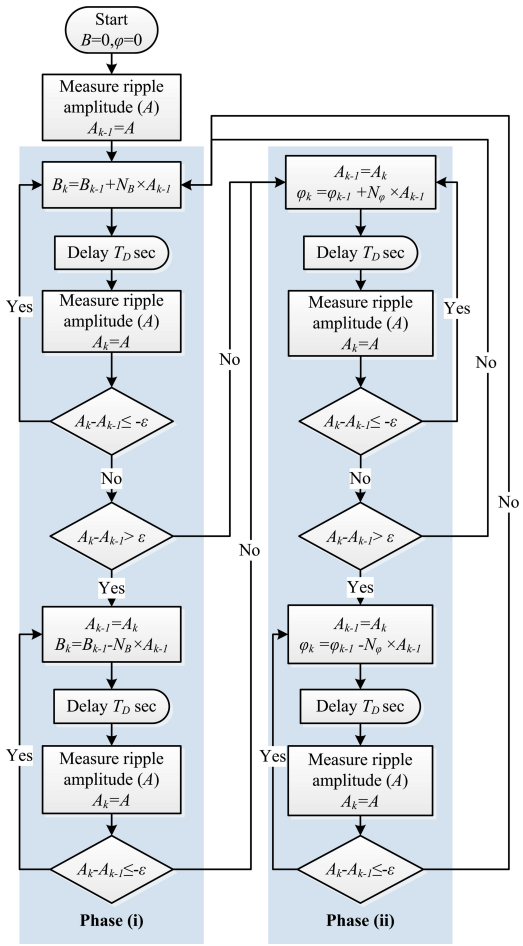

Fig. 7. Flow diagram of the proposed RBC for the second-order harmonic ripple current reduction.

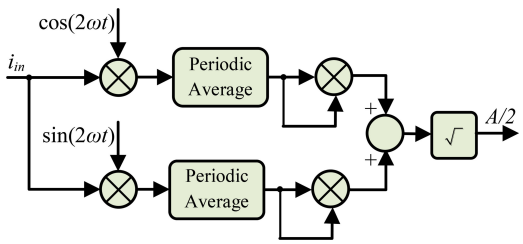

Fig. 8. Second-order harmonic ripple current amplitude measurement technique.

is simulated for various values of the inductor internal resistance and considering a $\pm 10\%$ change in C. A ripple reduction factor is defined as the ratio between the ripple current amplitude without and with the WFC method. Fig. 5 shows the ripple current reduction factor for various values of the inductor internal resistance and ± 10 % change in the capacitance of the output capacitors when the inverter supplies 10 W active power and 15 V Ar reactive power. Theoretically, a perfect ripple cancellation should result in an infinite ripple reduction factor. However, as it can be observed from Fig. 5, the capacitor tolerances and the inductor resistance cause significant performance degradation in the WFC method because it is based on direct calculation of the second-order harmonic reference voltage parameters. Hence, a control method which is able to generate the required second-order harmonic voltage reference signal parameters without calculating them from (26) and (27) can avoid the problem.

III. Proposed RBC for Ripple Current Mitigation

In this paper, a RBC is proposed to mitigate the second-order harmonic input ripple current component by adjusting the output capacitor second-order harmonic voltage reference amplitude B and phase angle φ. The main advantage of the proposed controller is that it can reduce the second-order harmonic ripple current in all four output power quadrants without being affected by the capacitor tolerances and the internal resistance of the inductors.

Variation of the second-order harmonic ripple current amplitude as a function of B and φ was analyzed for all four operating power quadrants to verify that it contains a global minimum. The results in Fig. 6 illustrate that the function contains a global minimum which corresponds to the B and φ values given by (20) and (21), respectively.

The proposed RBC incorporates a "perturb and observe" (P&O) approach [26], [27] to adjust the B and φ values. The flowchart of the proposed controller is shown in Fig. 7. Initially, both B and φ values are set to zero and the second-order harmonic ripple current amplitude A is measured. The controller operates in two phases. In the first phase, the value of B is either increased or decreased to reduce the ripple current component, and in the second phase, the value of φ is either increased or decreased to reduce the ripple current component. The transition between the phases occurs when a significant increment (ε) or decrement ($-\varepsilon$) of the ripple current amplitude cannot be obtained by increasing or decreasing either the value of B or φ (see Fig. 7).

Variable step size perturbations are used in the proposed controller algorithm in order to avoid design issues related to the fixed step size perturbations [26]. The variable step size perturbation method used for B is given by

$$B_k = B_{k-1} + N_B A_{k-1} \tag{45}$$

where N_B is a scalar, which is tuned at the design time of the controller and A is the measured second-order harmonic input current amplitude. Larger N_B results in faster dynamics with increased transition oscillations, while smaller N_B results in slower dynamics with smaller transition oscillations. Since the controller incorporates a P&O method, an increment of the second-order harmonic ripple current amplitude may occur due to the initial perturbation of B. N_B can be used to limit the initial ripple current amplitude change ΔA_{init} to a maximum allowable limit $\Delta A_{\text{init,max}}$. From (24), the maximum possible change of the second-order harmonic ripple current amplitude $\Delta A_{\max}$ due to a step change in B can be written as

$$\Delta A_{\max} = \frac{4C\omega V_d \Delta B_{\max}}{v_{\text{in}}} \tag{46}$$

where $\Delta B_{\max}$ is the maximum possible step change in B.

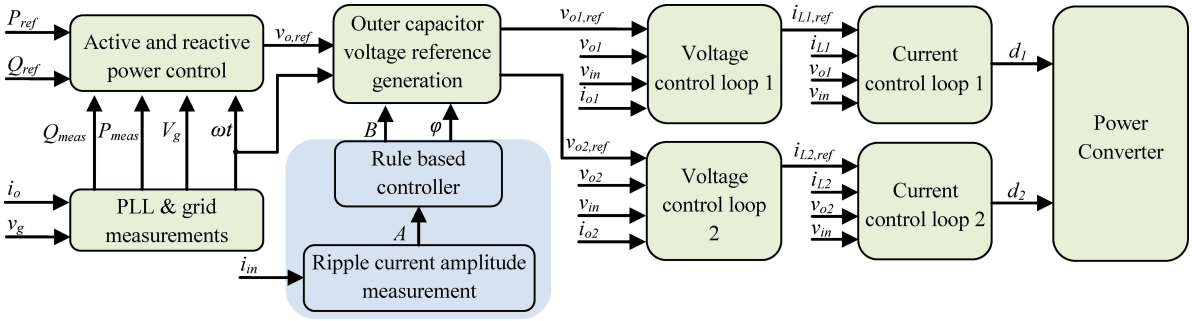

Fig. 9. Overall block diagram of the proposed control system.

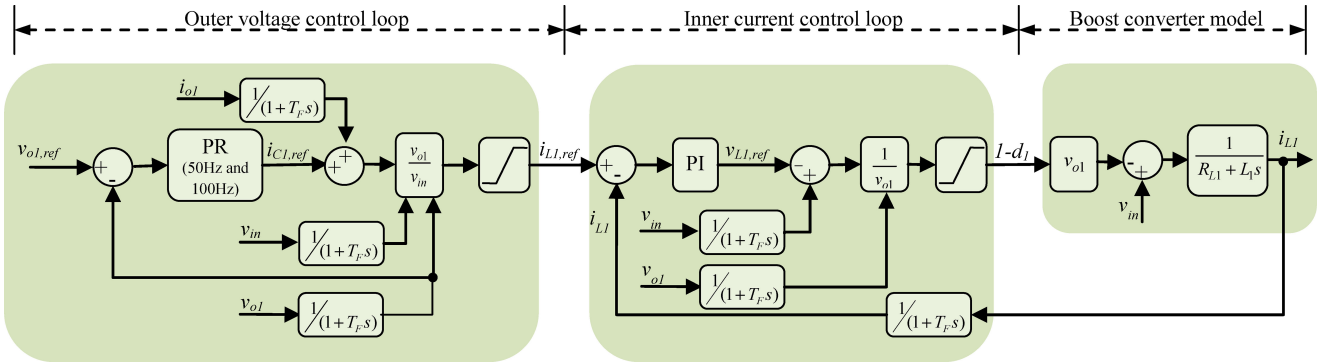

Fig. 10. Outer voltage control loop and inner current control loop for the left-hand side boost converter leg.

Hence, using (45) and (46), the value of N_{B} can be calculated to limit the initial step change of the ripple current amplitude ΔA_{init} due to the initial perturbation of B as

$$N_B = \left(\frac{v_{\mathrm{in}}}{4\omega C V_d}\right)\frac{\Delta A_{\mathrm{init,max}}}{A_{\mathrm{max}}} \tag{47}$$

where $\Delta A_{\mathrm{init,max}}$ is the maximum allowable initial step change of the ripple current amplitude and A_{max} is the maximum possible uncompensated second-order harmonic ripple current amplitude which is given by

$$A_{\mathrm{max}} = \frac{V_o}{2v_{\mathrm{in}}}\sqrt{\left[(I_{o,\mathrm{max}})^2 + \frac{C^2\omega^2 V_o^2}{4} + V_o I_{o,\mathrm{max}} C\omega\right]}. \tag{48}$$

The variable step size perturbation method used for φ is given by

$$\varphi_k = \varphi_{k-1} + N_\varphi A_{k-1} \tag{49}$$

where N_φ is a scalar, which is calculated for a maximum allowable phase-angle step change $\Delta\varphi_{\mathrm{max}}$ by

$$N_\varphi = \frac{\Delta\varphi_{\mathrm{max}}}{A_{\mathrm{max}}}. \tag{50}$$

There has to be a specific time delay T_D between each perturbation and the ripple amplitude measurement instant. The value of the required time delay T_D depends on the converter response time to a step change in the voltage reference and the time required to measure the second-order harmonic ripple amplitude accurately. The faster the measurement of the second-order harmonic ripple current amplitude, the faster the dynamic performance of the controller. Hence, a fast Fourier transformation based amplitude measurement technique [28] is employed to ensure fast and accurate measurement. Fig. 8 shows the block diagram of the second-order harmonic ripple current amplitude measurement system. From (24), the total input current of the boost inverter with modified output capacitor reference

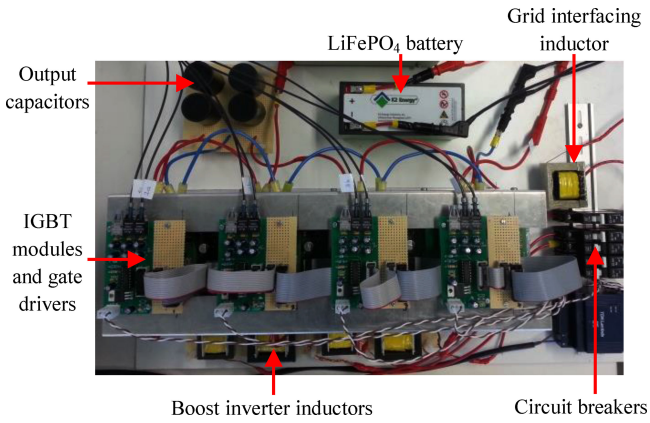

Fig. 11. Experimental prototype of the single-phase DC/AC boost inverter-based battery storage system.

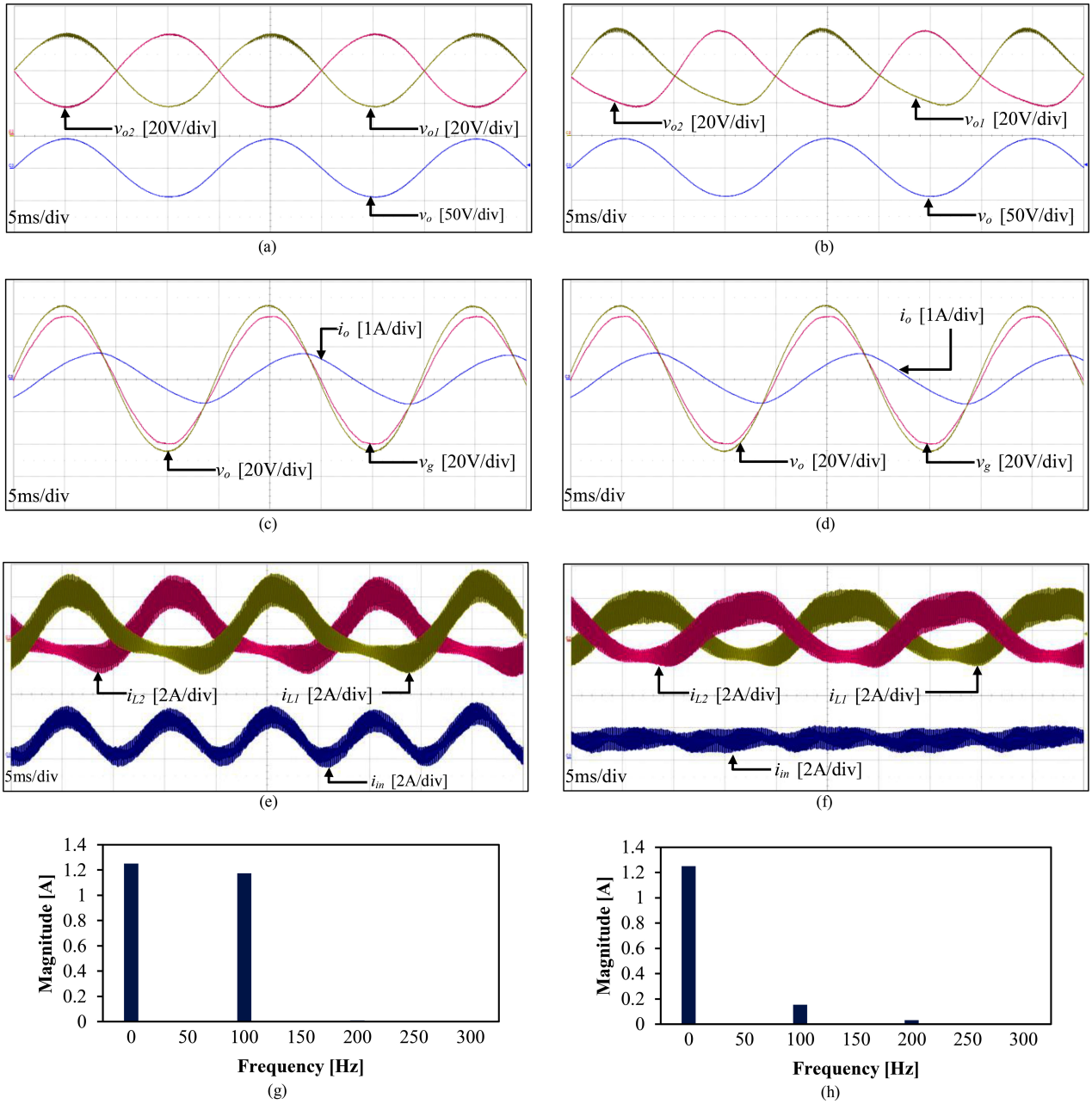

Fig. 12. Experimental results illustrating operation of the battery storage system when delivering 15 V Ar reactive power and 10 W active power. (a) Output capacitor voltage waveforms and inverter output voltage without the RBC. (b) Output capacitor voltage waveforms and inverter output voltage with the RBC. (c) Inverter output voltage, grid voltage, and inverter output current without the RBC. (d) Inverter output voltage, grid voltage, and inverter output current with the RBC. (e) Inductor currents and total input current of the boost inverter without the RBC. (f) Inductor currents and total input current of the boost inverter with the RBC. (g) Frequency characteristics of the input current without the RBC. (h) Frequency characteristics of the input current with the RBC.

signals consists of a DC component, a second-order harmonic component, and a fourth-order harmonic component. The total boost inverter input current in (24) can be rewritten as

$$i_{\text{in}} = I_{\text{in,DC}} + I_{\text{in},2\omega}\cos(2\omega t + \gamma_{2\omega}) + I_{\text{in},4\omega}\cos(4\omega t + \gamma_{4\omega}). \quad (51)$$

The following equations can be obtained after multiplying (51) with the reference signals $\cos(2\omega t)$ and $\sin(2\omega t)$

$$i_{\text{in}}\cos(2\omega t) = I_{\text{in,DC}}\cos(2\omega t) + I_{\text{in},2\omega}\left[\frac{\cos(\gamma_{2\omega}) + \cos(4\omega t + \gamma_{2\omega})}{2}\right] + I_{\text{in},4\omega}\left[\frac{\cos(2\omega t + \gamma_{4\omega}) + \cos(6\omega t + \gamma_{4\omega})}{2}\right] \quad (52)$$

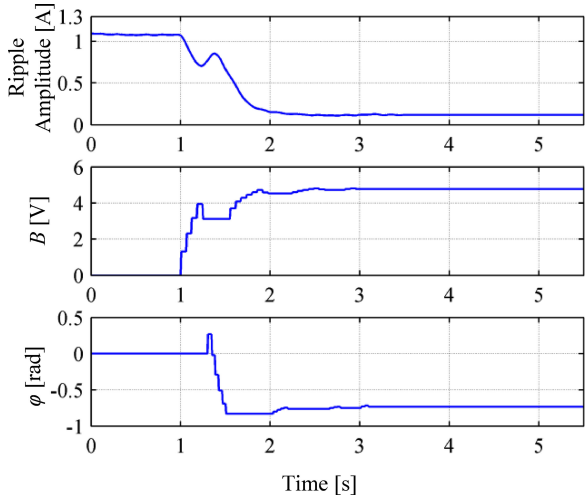

Fig. 13. Experimental results illustrating operation of the proposed RBC when the battery storage system supplies 10 W active power and 15 V Ar reactive power.

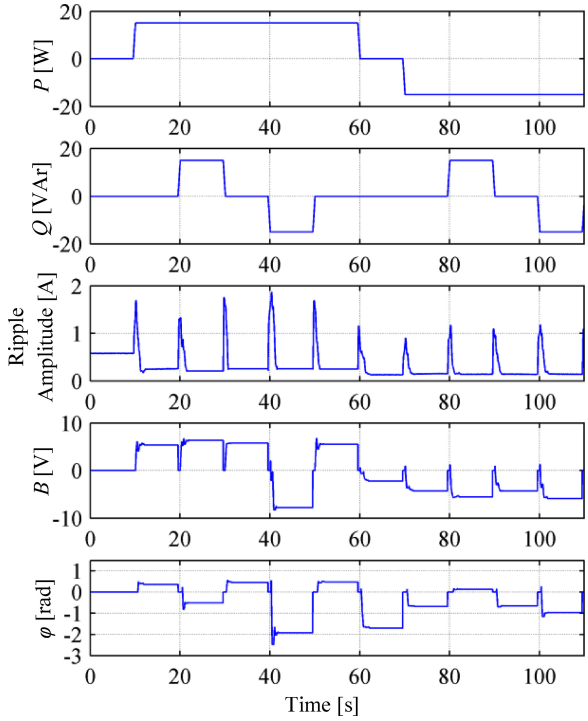

Fig. 14. Operation of the RBC with step-changing inverter output power.

$$i_{\text{in}}\sin(2\omega t) = I_{\text{in,DC}}\sin(2\omega t) + I_{\text{in},2\omega}\left[\frac{\sin(\gamma_{2\omega}) + \sin(4\omega t + \gamma_{2\omega})}{2}\right] + I_{\text{in},4\omega}\left[\frac{\sin(2\omega t + \gamma_{4\omega}) + \sin(6\omega t + \gamma_{4\omega})}{2}\right]. \tag{53}$$

By averaging (52) and(53) over a period of the second-order harmonic waveform (T_{avg}), the following equations can be obtained:

$$i_{\text{in}}\cos(2\omega t)_{\text{avg}} = \frac{1}{T_{\text{avg}}}\int_0^{T_{\text{avg}}} i_{\text{in}}\cos(2\omega t)dt = \frac{I_{\text{in},2\omega}\cos(\gamma_{2\omega})}{2} \tag{54}$$

$$i_{\text{in}}\sin(2\omega t)_{\text{avg}} = \frac{1}{T_{\text{avg}}}\int_0^{T_{\text{avg}}} i_{\text{in}}\sin(2\omega t)dt = \frac{I_{\text{in},2\omega}\sin(\gamma_{2\omega})}{2}. \tag{55}$$

Then, the second-order harmonic ripple current amplitude can be obtained as

$$A = 2\sqrt{(i_{\text{in}}\cos(2\omega t)_{\text{avg}})^2 + (i_{\text{in}}\sin(2\omega t)_{\text{avg}})^2}. \tag{56}$$

The method requires T_{avg} time to accurately measure the ripple current amplitude. Hence, for the proper operation of the RBC, the delay time between the perturbations and the measurements T_D has to be selected such that

$$T_D \geq T_{\text{avg}}. \tag{57}$$

To avoid possible steady-state oscillations, the controller should be disabled after a predetermined number of iterations.

IV. Boost Inverter Control System

The overall block diagram of the grid-connected boost inverter with the proposed RBC is shown in Fig. 9. The parameters of the experimental prototype are summarized in Table I.

Two double-loop controllers are implemented to control the output capacitor voltages v_{o1} and v_{o2}, as given by (20) and (21), respectively. Each double-loop controller has an inner current control loop and an outer voltage control loop. The block diagram of the double-loop controller for the left-hand side boost converter leg is shown in Fig. 10. A proportional resonant (PR) controller with two resonant components which are tuned to 50 and 100 Hz is employed in the voltage control loop to achieve better sinusoidal reference following [29]. The transfer function of the PR controller is given by

$$H_{\text{PR}}(s) = K_p + \frac{2K_{i1}\omega_{c1}s}{s^2 + 2\omega_{c1}s + \omega_1^2} + \frac{2K_{i2}\omega_{c2}s}{s^2 + 2\omega_{c2}s + \omega_2^2} \tag{58}$$

where K_p, K_{i1}, and K_{i2} are gains of the PR controller. The bandwidth of the resonant components can be adjusted using ω_{c1} and ω_{c2}. The parameters ω_1 and ω_2 are selected as 314.2 and 628.3 rads^{-1}, respectively. The proportional-integral (PI) controller-based inner current control loops are designed for each boost converter leg using the average continuous time model of the boost converter. The PR controllers for the outer voltage control loops are designed with 400 Hz bandwidth and the PI controllers for the inner current control loops are designed with 4 kHz bandwidth. Both loops are designed to achieve at least 50° phase margin [23].

Interleaved operation for the boost inverter topology proposed in [19] was adopted in this paper to reduce the switching frequency ripple current.

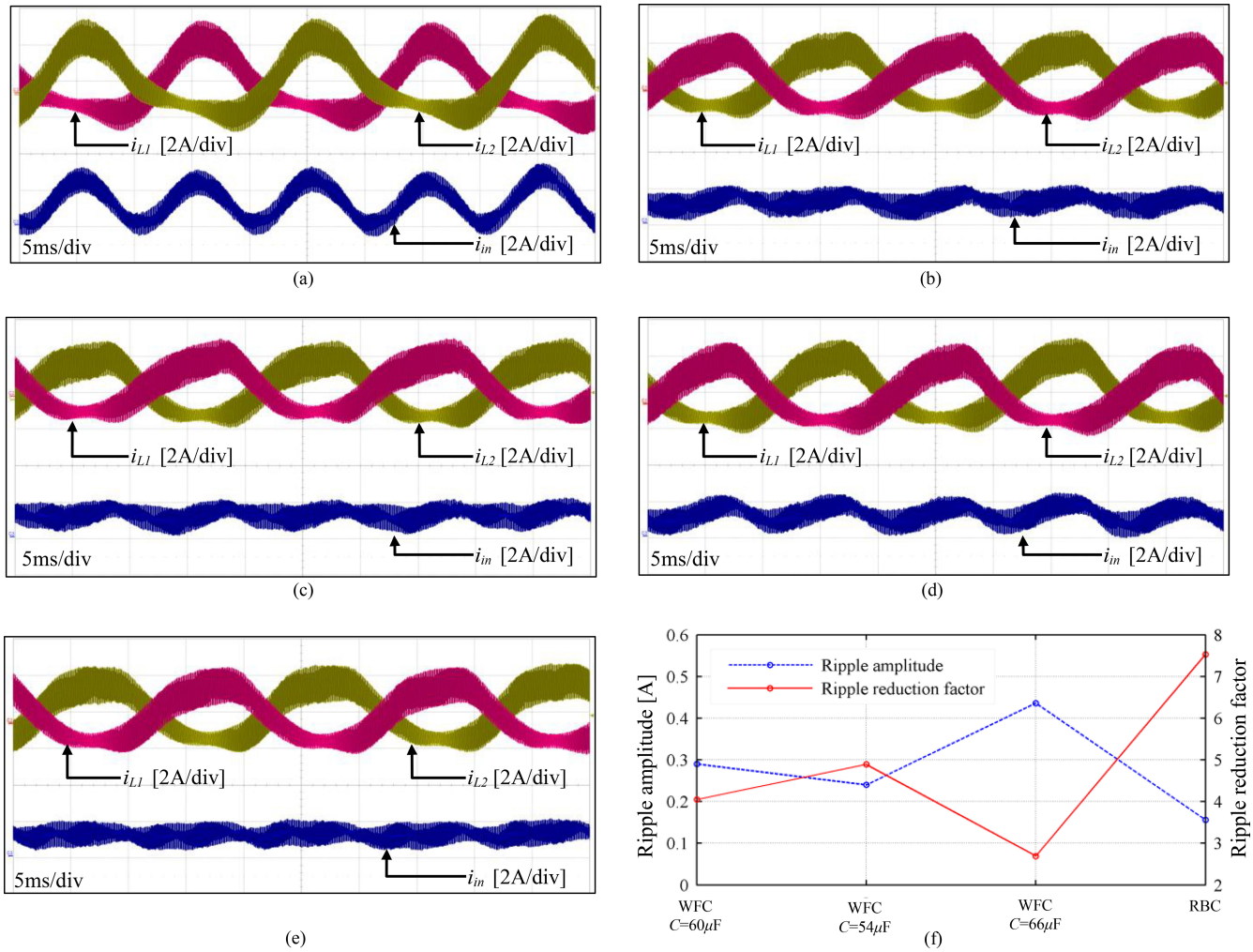

Fig. 15. Experimental results illustrating the effect of capacitor tolerances on the ripple current reduction when the WFC method is used. (a) Inductor currents and total input current of the boost inverter without any ripple current reduction method. (b) Inductor currents and total input current of the boost inverter with the WFC method and $C = 60$ μF. (c) Inductor currents and total input current of the boost inverter with the WFC method and $C = 54$ μF. (d) Inductor currents and total input current of the boost inverter with the WFC method and $C = 66$ μF. (e) Inductor currents and total input current of the boost inverter with the RBC. (f) Comparison of the ripple amplitude and ripple reduction factor for cases (b)–(e).

Two PI controllers are designed to control the active and reactive power exchanged with the grid based on (9) and (10). A second-order generalized integrator [30] based phase-locked loop (PLL) is used for the grid synchronization and power measurements. The active and reactive power PI controllers are designed to have at least 0.1s rise time to ensure proper output power reference tracking.

The maximum possible uncompensated second-order harmonic input current amplitude $A_{\max}$ can be calculated using (48). The scalar N_B for the RBC is calculated such that the maximum initial step change of the second-order harmonic ripple component is 25% of the maximum possible uncompensated second-order harmonic input current amplitude $A_{\max}$. The scalar N_φ for the RBC is selected such that the maximum possible step change of the phase angle φ is $0.75\ \mathrm{rads}^{-1}$. A large value for ε can reduce the ripple reduction performance of the controller, while a very small ε can lead to slower dynamics. Hence, ε was selected as 0.01 to achieve better ripple reduction with faster dynamics. All controller parameters for the experimental prototype are summarized in Table I.

V. Experimental Results

The proposed RBC for the single-phase grid-connected boost inverter was verified using an experimental prototype shown in Fig. 11. A 6.4 Ah, 12.8 V $LiFePO_4$ battery was used as the input power source. MATLAB/Simulink was used to implement the controller on a DSpace DS1006 platform. Parameters of the control system are summarized in the Table I. The BESS was connected to the AC grid through a step-up transformer.

Fig. 12 shows the operation of the grid-connected boost inverter without and with the proposed ripple current reduction method. The inverter is controlled to deliver 10 W active power and 15 V Ar reactive power to the grid. Fig. 12(a) and (b) shows the waveforms of the output capacitor voltages and the inverter output voltage, without and with the rule-based control, respectively. As expected, the output voltage waveform is the same

TABLE II
SECOND-ORDER HARMONIC RIPPLE CURRENT MITIGATION FOR VARIOUS OUTPUT POWER CONDITIONS

Active power [W]	Reactive power [V·Ar]	Ripple amplitude without any compensation method [A]	Ripple amplitude reduction factor with RBC	Ripple amplitude reduction factor with WFC method
20	0	1.954	6.65	5.4
–20	0	1.067	6.28	5.1
0	15	0.605	6.80	3.3
0	–15	1.343	7.07	4.83
15	10	1.454	7.09	4.0
15	–10	1.843	7.26	5.2
–15	10	0.936	7.04	4.7
–15	–10	1.114	7.38	5.9
10	15	1.174	7.50	4.04

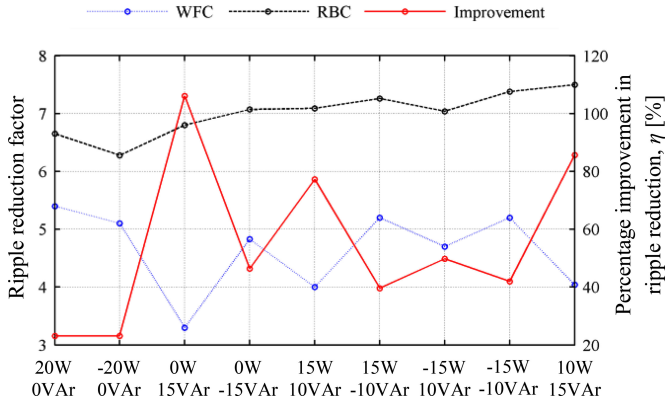

Fig. 16. Comparison of the ripple current reduction using the WFC method and the RBC.

despite the difference in the output capacitor voltage waveforms. Fig. 12(c) and (d) depicts the inverter output voltage, grid voltage, and the output current waveforms. Both the active and reactive powers supplied to the grid are controlled by changing the amplitude and phase angle of the inverter output voltage with respect to the grid voltage. The inductor current waveforms and the total input current waveforms of the boost inverter without and with the rule-based control are shown in the Fig. 12(e) and (f), respectively. Significant reduction in the DC-side current ripple component can be observed after applying the RBC compared to the conventional operation of the boost inverter.

The frequency spectrum characteristics of the boost inverter input current are shown in Fig. 12(g) and (h) for both cases. The second-order harmonic component amplitude with conventional operation is 1.174 A, while the second-order harmonic current component amplitude with the RBC is reduced to 0.156 A achieving close to 7.5 times reduction in the second-order harmonic ripple current amplitude. The fourth-order harmonic current component with the proposed controller is 32 mA, while it is 11 mA with the conventional operation. The increment in the fourth-order harmonic current component is as expected due to modification in the output capacitor reference voltages. However, the effect of the increment in the fourth-order harmonic current component is negligible compared to the reduction in the second-order harmonic input current component.

Dynamic performance of the RBC is shown in Fig. 13. The controller is enabled at the time 1 s. First, the value of B is adjusted to reduce the second-order harmonic ripple current amplitude followed by a phase angle φ adjustment. After several iterations, significant ripple current reduction is achieved. To avoid steady-state oscillations, the controller is disabled after four cycles.

Performance of the proposed controller for a step change in the output active and reactive power is shown in Fig. 14. The RBC is reactivated each time, a change in the reference active or reactive power $P_{\rm ref}$, $Q_{\rm ref}$ occurs. Since it takes about 2 s to perform the P&O process, this time interval limits how frequently the change in the reference active or reactive power can occur.

To emulate the effect of the capacitor tolerances on the input current ripple reduction, the capacitance value used for the second-order harmonic voltage reference parameter calculation was changed by $\pm 10\%$ from the nominal capacitor value 60 μF. Fig. 15 illustrates the effect of the change in the capacitance value on the second-order harmonic ripple current reduction when the WFC method is used. For the considered output power operating point (10 W active power and 15 V Ar reactive power), a –10% change in capacitance does not leads to a significant change in the ripple reduction. However, a $+10\%$ change in the capacitance value results in considerable reduction in the waveform controller performance.

Since the boost inverter second-order harmonic input current amplitude and phase angle vary with the inverter output power, the operation of the proposed controller was tested in all possible output power operating quadrants. The boost inverter input current ripple reductions obtained using the WFC method and the proposed rule-based control method are compared for all possible output power conditions in Table II and illustrated in Fig. 16. A comparison of input current waveforms without and with the proposed RBC in all four output power quadrants is shown in Fig. 17. It can be observed that the proposed RBC is able to reduce the ripple current at least six times in all conditions, while the WFC method fails to achieve the significant ripple current reduction at some of the output power conditions. Percentage improvement in the ripple reduction η when using the RBC as compared with the WFC method is also illustrated in Fig. 16

$$\eta = \frac{R_{\rm RBC} - R_{\rm WFC}}{R_{\rm WFC}} \times 100\% \tag{59}$$

where $R_{\rm RBC}$ and $R_{\rm WFC}$ are the ripple reduction factors obtained from the rule-based control method and the WFC method, respectively.

VI. CONCLUSION

In conventional single-phase DC/AC boost inverter-based ESSs, a second-order harmonic current ripple exists at the DC side of the inverter. The ripple current increases the internal heating and losses in the connected DC energy storage devices

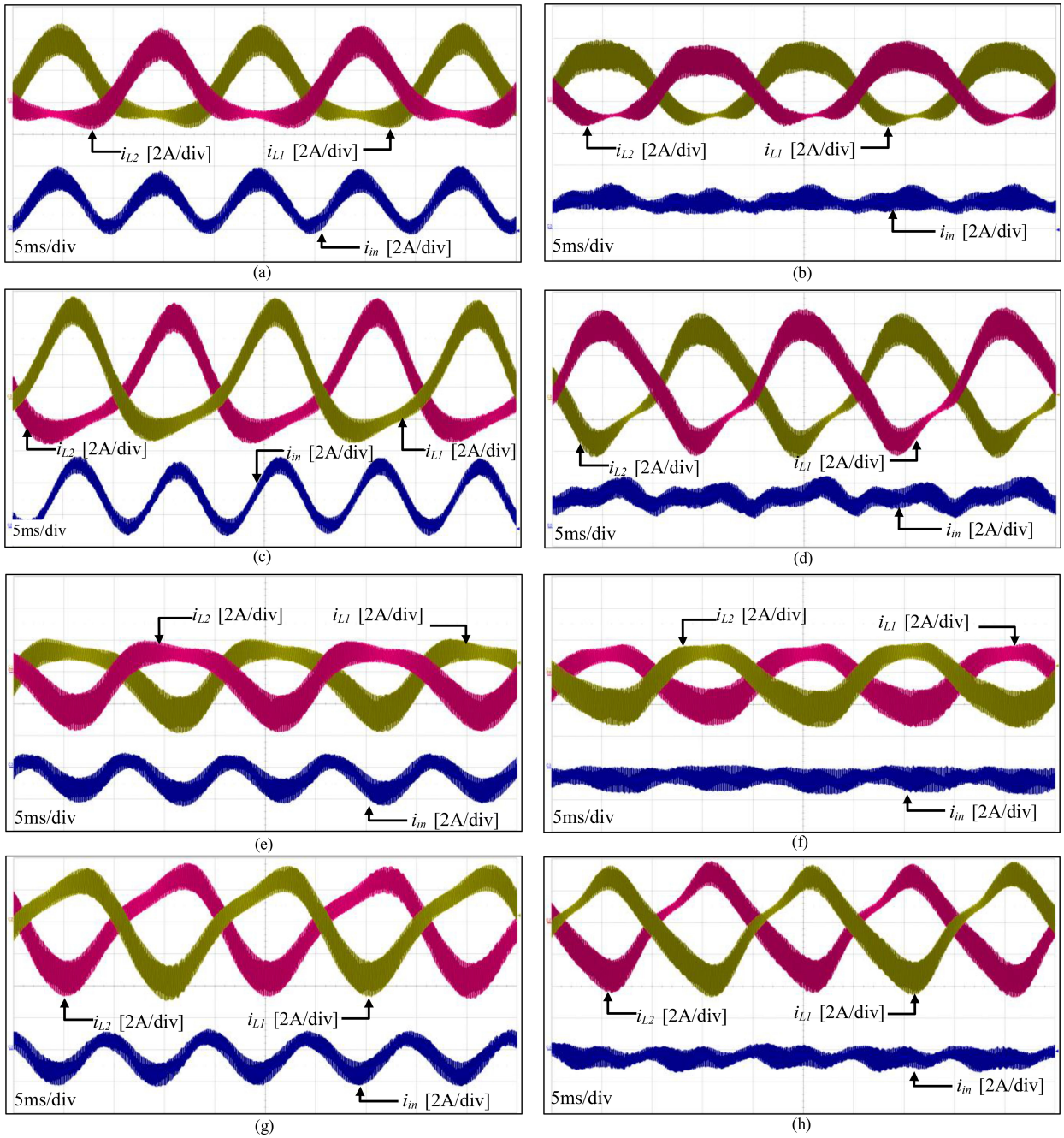

Fig. 17. Experimental results comparing the inductor current and input current waveforms without and with the proposed RBC. Inductor currents and total input current of the boost inverter when $P = 15$ W and $Q = 10$ V·Ar (a) without the RBC and (b) with the controller. Inductor currents and total input current of the boost inverter when $P = 15$ W and $Q = -10$ V·Ar (c) without the RBC and (d) with the controller. Inductor currents and total input current of the boost inverter when $P = -15$ W and $Q = 10$ V·Ar (e) without the RBC and (f) with the controller. Inductor currents and total input current of the boost inverter when $P = -15$ W and $Q = -10$ V·Ar (g) without the RBC and (h) with the controller.

and degrades their lifetime. Therefore, in order to improve the lifetime of the ESSs, mitigation of the ripple current is of great importance. In this paper, it was shown that the effect of the inductor internal resistance and the output capacitor tolerances can significantly degrade performance of the WFC method. Herein, a RBC to mitigate the second-order harmonic input current ripple was proposed and experimentally verified. It was confirmed that the RBC can achieve better ripple current reduction as compared to the WFC approach without its performance being affected by the capacitor tolerances and the inductor internal resistance.

REFERENCES

[1] Q. Hao, Z. Jianhui, L. Jih-Sheng, and Y. Wensong, "A high-efficiency grid-tie battery energy storage system," *IEEE Trans. Power Electron.*, vol. 26, no. 3, pp. 886–896, Mar. 2011.

[2] C. A. Hill, M. C. Such, C. Dongmei, J. Gonzalez, and W. M. Grady, "Battery energy storage for enabling integration of distributed solar power generation," *IEEE Trans. Smart Grid*, vol. 3, no. 2, pp. 850–857, Jun. 2012.

[3] A. Kuperman, U. Levy, J. Goren, A. Zafransky, and A. Savernin, "Battery charger for electric vehicle traction battery switch station," *IEEE Trans. Ind. Electron.*, vol. 60, no. 12, pp. 5391–5399, Dec. 2013.
[4] P. Sung-Yeul, C.-L. Chen, and L. Jih-Sheng, "A wide-range active and reactive power flow controller for a solid oxide fuel cell power conditioning system," *IEEE Trans. Power Electron.*, vol. 23, no. 6, pp. 2703–2709, Nov. 2008.
[5] J. Wu, X. Z. Yuan, J. J. Martin, H. Wang, J. Zhang, and J. Shen, "A review of PEM fuel cell durability: Degradation mechanisms and mitigation strategies," *J. Power Sources*, vol. 184, pp. 104–119, Sep. 15, 2008.
[6] R. Ferrero, M. Marracci, and B. Tellini, "Single PEM fuel cell analysis for the evaluation of current ripple effects," *IEEE Trans. Instrum. Meas.*, vol. 62, no. 5, pp. 1058–1064, May 2013.
[7] A. J. Ruddell, A. G. Dutton, H. Wenzl, C. Ropeter, D. U. Sauer, and J. Merten, "Analysis of battery current microcycles in autonomous renewable energy systems," *J. Power Sources*, vol. 112, pp. 531–546, Nov. 14, 2002.
[8] S. Bala, T. Tengner, P. Rosenfeld, and F. Delince, "The effect of low frequency current ripple on the performance of a lithium iron phosphate (LFP) battery energy storage system," in *Proc. IEEE Energy Convers. Congr. Expo.*, 2012, pp. 3485–3492.
[9] R. A. Dougal, S. Liu, and R. E. White, "Power and life extension of battery-ultracapacitor hybrids," *IEEE Trans. Compon. Packag. Technol.*, vol. 25, no. 1, pp. 120–131, Mar. 2002.
[10] Z. Haihua, T. Bhattacharya, T. Duong, T. S. T. Siew, and A. M. Khambadkone, "Composite energy storage system involving battery and ultracapacitor with dynamic energy management in microgrid applications," *IEEE Trans. Power Electron.*, vol. 26, no. 3, pp. 923–930, Mar. 2011.
[11] Product guide—Maxwell technologies BOOSTCAP ultracapacitors, Maxwell Technologies, San Diego, CA, USA, 2009.
[12] J. Minsoo and V. G. Agelidis, "A minimum power-processing-stage fuel-cell energy system based on a boost-inverter with a bidirectional backup battery storage," *IEEE Trans. Power Electron.*, vol. 26, no. 5, pp. 1568–1577, May 2011.
[13] J. Minsoo, M. Ciobotaru, and V. G. Agelidis, "A single-phase grid-connected fuel cell system based on a boost-inverter," *IEEE Trans. Power Electron.*, vol. 28, no. 1, pp. 279–288, Jan. 2013.
[14] Z. Guo-Rong, X. Cheng-Yuan, W. Hao-Ran, C. Wei, and T. Siew-Chong, "Dynamic characteristics of boost inverter with waveform control," in *Proc. IEEE 29th Annu. Appl. Power Electron. Conf. Expo.*, 2014, pp. 1771–1775.
[15] Z. Guo-Rong, T. Siew-Chong, W. Ke-Wei, and C. K. Tse, "Waveform control of fuel-cell inverter systems," in *Proc. IEEE Energy Convers. Congr. Expo.*, 2012, pp. 4457–4463.
[16] Z. Guo-Rong, T. Siew-Chong, C. Yu, and C. K. Tse, "Mitigation of low-frequency current ripple in fuel-cell inverter systems through waveform control," *IEEE Trans. Power Electron.*, vol. 28, no. 2, pp. 779–792, Feb. 2013.
[17] G. R. Zhu, H. R. Wang, C. Y. Xiao, T. Siew-Chong, and Y. Kang, "Assessment of waveform control method for mitigation of low-frequency current ripple," in *Proc. IEEE 28th Annu. Appl. Power Electron. Conf. Expo.*, 2013, pp. 3101–3106.
[18] H. R. Wang, G. R. Zhu, X. B. Fu, W. X. Liu, C. Y. Xiao, and B. Liang, "Mitigating low frequency ripple in multiply micro sources inverter system with waveform control method," in *Proc. IEEE 23rd Int. Symp. Ind. Electron.*, 2014, pp. 2390–2394.
[19] D. B. Wickramasinghe Abeywardana, B. Hredzak, and V. G. Agelidis, "Single-phase grid-connected LiFePO4 battery-supercapacitor hybrid energy storage system with interleaved boost inverter," *IEEE Trans. Power Electron.*, vol. PP, no. 99, p.1, 2014, doi: 10.1109/TPEL.2014.2372774.
[20] L. Changrong and L. Jih-Sheng, "Low frequency current ripple reduction technique with active control in a fuel cell power system with inverter load," *IEEE Trans. Power Electron.*, vol. 22, no. 4, pp. 1429–1436, Aug. 2007.
[21] W. Jianhua, J. Baojian, L. Xuqian, D. Xiang, Z. Fanghua, and G. Chunying, "Steady-state and dynamic input current low-frequency ripple evaluation and reduction in two-stage single-phase inverters with back current gain model," *IEEE Trans. Power Electron.*, vol. 29, no. 8, pp. 4247–4260, Aug. 2014.
[22] A. Ale Ahmad, A. Abrishamifar, and S. Samadi, "Low-frequency current ripple reduction in front-end boost converter with single-phase inverter load," *IET Power Electron.*, vol. 5, pp. 1676–1683, 2012.
[23] P. Sanchis, A. Ursaea, E. Gubia, and L. Marroyo, "Boost DC-AC inverter: A new control strategy," *IEEE Trans. Power Electron.*, vol. 20, no. 2, pp. 343–353, Mar. 2005.
[24] R. Teodorescu, M. Liserre, and P. Rodríguez, *Grid Converters for Photovoltaic and Wind Power Systems.* Hoboken, NJ, USA: Wiley, 2011.
[25] L. Hongbo, Z. Kai, Z. Hui, F. Shengfang, and X. Jian, "Active power decoupling for high-power single-phase PWM rectifiers," *IEEE Trans. Power Electron.*, vol. 28, no. 3, pp. 1308–1319, Mar. 2013.
[26] L. Fangrui, D. Shanxu, L. Fei, L. Bangyin, and K. Yong, "A variable step size INC MPPT method for PV systems," *IEEE Trans. Ind. Electron.*, vol. 55, no. 7, pp. 2622–2628, Jul. 2008.
[27] N. Femia, G. Petrone, G. Spagnuolo, and M. Vitelli, "Optimization of perturb and observe maximum power point tracking method," *IEEE Trans. Power Electron.*, vol. 20, no. 4, pp. 963–973, Jul. 2005.
[28] L. Kyoung-Jun, L. Jong-Pil, S. Dongsul, Y. Dong-Wook, and K. Hee-Je, "A novel grid synchronization PLL method based on adaptive low-pass notch filter for grid-connected pcs," *IEEE Trans. Ind. Electron.*, vol. 61, no. 1, pp. 292–301, Jan. 2014.
[29] R. Teodorescu, F. Blaabjerg, M. Liserre, and P. C. Loh, "Proportional-resonant controllers and filters for grid-connected voltage-source converters," *IEE Proc. Electric Power Appl.*, vol. 153, no. 5, pp. 750–762, Sep. 2006.
[30] M. Ciobotaru, V. G. Agelidis, R. Teodorescu, and F. Blaabjerg, "Accurate and less-disturbing active antiislanding method based on PLL for grid-connected converters," *IEEE Trans. Power Electron.*, vol. 25, no. 6, pp. 1576–1584, Jun. 2010.

Damith B. Wickramasinghe Abeywardana (S'12) received the B.Sc. degree in electrical and electronic engineering from the University of Peradeniya, Peradeniya, Sri Lanka. He is currently working toward the Ph.D. degree in electrical engineering and telecommunications with the University of New South Wales, Sydney, Australia.

His research interests include hybrid energy storage systems, renewable energy integration, and smart grids. His research is also involved with the Australian Energy Research Institute, Sydney.

Branislav Hredzak (M'98–SM'13) received the B.Sc./M.Sc. degree from the Technical University of Kosice, Kosice, Slovakia, in 1993, and the Ph.D. degree from the Napier University of Edinburgh, Edinburgh, U.K., in 1997, all in electrical engineering.

He was as a Lecturer and a Senior Researcher in Singapore from 1997 to 2007. He is currently a Senior Lecturer at the School of Electrical Engineering and Telecommunications, The University of New South Wales, Sydney, N.S.W., Australia. His current research interests include hybrid storage technologies and advanced control systems for power electronics and storage systems

Vassilios G. Agelidis (SM'00) was born in Serres, Greece. He received the B.Eng. degree in electrical engineering from the Democritus University of Thrace, Thrace, Greece, in 1988, the M.S. degree in applied science from Concordia University, Montreal, QC, Canada, in 1992, and the Ph.D. degree in electrical engineering from Curtin University, Perth, Australia, in 1997.

He was with Curtin University from 1993 to 1999, the University of Glasgow, Glasgow, U.K., from 2000 to 2004, Murdoch University, Perth, from 2005 to 2006, and the University of Sydney, Sydney, Australia, from 2007 to 2010. He is currently the Director of the Australian Energy Research Institute, University of New South Wales, Sydney.

Dr. Agelidis received the Advanced Research Fellowship from the U.K.'s Engineering and Physical Sciences Research Council in 2004. He was the Vice President Operations within the IEEE Power Electronics Society from 2006 to 2007. He was an AdCom Member of the IEEE Power Electronics Society from 2007 to 2009 and the Technical Chair of the 39th IEEE Power Electronics Specialists Conference, 2008, Rhodes, Greece.